OPEN ACCESS

Ni/GDC Fuel Electrode for Low-Temperature SOFC and its Aging Behavior Under Accelerated Stress

To cite this article: Y. Liu *et al* 2024 *J. Electrochem. Soc.* **171** 054514

Journal of The Electrochemical Society, 2024 **171** 054514

Ni/GDC Fuel Electrode for Low-Temperature SOFC and its Aging Behavior Under Accelerated Stress

Y. Liu,[1,z] M. Juckel,[2] N. H. Menzler,[2] and A. Weber[1,*]

[1]*Institute for Applied Materials (IAM-ET), Karlsruhe Institut of Technologie (KIT), Karlsruhe 76131, Germany*
[2]*Institute of Energy and Climate Research (IEK), IEK-1: Materials Synthesis and Processing, Forschungszentrum Jülich GmbH, Jülich 52425, Germany*

The microstructural integrity of Ni-based fuel electrodes is important for long-term solid oxide fuel cell (SOFC) operation. Degradation due to microstructural changes such as Ni-agglomeration, coarsening, and densification must be prevented by an appropriate microstructure. Here, the performance of four types of nickel-ceria-based fuel electrodes, which differ concerning layer sequence and manufacturing processes, was evaluated by electrochemical impedance spectroscopy at the nominal operating temperature of 600 °C. Electrodes produced through screen-printed GDC exhibited an acceptable polarization resistance (0.260 Ωcm^2), whereas electrodes with an additional printed Ni/GDC layer demonstrated inferior performance (0.550 Ωcm^2). Electrodes formed through infiltration of GDC into the printed GDC-layer displayed unreproducible performance values ranging from 0.16 to 1.20 Ωcm^2 despite similar processing. Conversely, electrodes with an extra layer of GDC infiltrated into the Ni-backbone exhibited good performance (0.195 Ωcm^2) and stability. Accelerated degradation tests under OCV at increased operating temperatures of 700 and 900 °C were performed on the sample based on a GDC infiltrated Ni-backbone that performed best among reproducible samples. The polarization resistance at 600 °C recorded at the beginning and the end of life increased by up to 100%. Microstructural analysis of the electrodes at different aging states revealed strong microstructural changes of fine-infiltrated GDC structures and Ni agglomeration at higher operating temperature.
 [DOI: 10.1149/1945-7111/ad4917]

Manuscript submitted January 9, 2024; revised manuscript received March 25, 2024. Published May 17, 2024. *This paper is part of the JES Focus Issue on SOFC XVIII: Advances in Solid Oxide Fuel Cell and Electrolysis Cell Technology.*

List of Symbols

H_2	hydrogen
H_2O	water steam
H_2S	hydrogen sulfide
He	helium
HF	high frequency process at fuel electrode (−)
$(Gd_{0.1}Ce_{0.9})(NO_3)_3$	an aqueous solution of gadolinium-doped cerium nitrate
LFi	low frequency process i at fuel electrode (−)
MF	middle frequency process at fuel electrode (−)
H2	nitrogen
NiO	nickel oxide
p_i	partial pressure of the component i (atm)
R_{LF_2}	fit resistance of the process LF_2 (Ωcm^2)
t	time (s)
T	temperature (K)
Y_2O_3	yttrium oxide
ZrO_2	zirconium dioxide

The commercialization of Solid Oxide Fuel Cells (SOFC) demands reduced costs and extended system lifetimes.[1] Operating at lower temperatures (<650 °C) facilitates a broader selection of (cost-effective) materials and enhances system stability. However, performance significantly decreases as the temperature drops due to the low conductivity of commonly used electrolytes, such as yttria-stabilized zirconia (YSZ), resulting in high ohmic resistance. The polarization resistance of both electrodes also increases due to the thermal activation of electrochemical processes.[2] To achieve outstanding performance and stability at intermediate temperatures, new materials and production methods for improved cell structures are necessary.[3]

Ni/YSZ cermet fuel electrodes, prepared by conventional ceramic processing, face challenges in achieving high performance at the lower temperatures.[3] The limited purely ionic conductivity of YSZ restricts its use at lower operating temperatures.[4] Another challenge with Ni/YSZ is anode poisoning due to sulfur compounds present in almost all available fuels.[5,6] A 5-fold increase in the polarization resistance of Ni/YSZ anodes was observed after exposure to small amounts of H_2S (less than 1 ppm).[7,8] Previous studies have shown that sulfur occupied the Ni surface, reducing its activity as an electrocatalyst or sole catalyst for hydrogen electrooxidation at the three-phase boundary (TPB) or water-gas shift reaction (WGS).[7–9] In comparison, Ni/ceria anodes demonstrate superiority in both aspects. Particularly at temperatures as low as 500 °C, the ionic conductivity of gadolinia-doped ceria (GDC) is significantly higher than that of YSZ.[4] The enhanced tolerance of this kind of anode against sulfur poisoning has been demonstrated several times and is attributed to the property of GDC as a mixed-ionic-electronic-conducting (MIEC) material. The reaction is not solely limited to TPB but also possible at the GDC pore interface.[10–12]

Presently available Ni/GDC fuel electrodes do not exhibit sufficient performance at 600 °C (polarization resistance: 0.800 Ωcm^2 at 600 °C[13]), as they are developed for electrolyte-supported cells targeting operating temperatures of 750 to 900 °C. Their coarse microstructures provide sufficient performance at the targeted operating temperatures, and possess excellent durability under these conditions.

To enhance anode performance, wet infiltration is a highly effective method. In the previous study by our group,[9] different nickel/ceria cermet anodes were tested. The Ni/GDC layer printed directly on an 8 mol% Y_2O_3 stabilized ZrO_2 (8YSZ) electrolyte exhibited the highest initial polarization resistance and the lowest sulfur tolerance, with an increase of more than 300% in polarization resistance upon exposure to sulfur. The initial polarization resistance dropped below 200 $m\Omega cm^2$ after the infiltration of Ni, cerium dioxide solution, or a mixture of Ni/cerium dioxide solutions. Its polarization resistance increase due to sulfur was only 20%.[9] Mitchell-Williams et al.[14] infiltrated GDC particles into commercially available anode-supported SOFC (NiO-8YSZ/8YSZ/lanthanum strontium cobalt ferrite (LSCF)) by inkjet printing. The infiltration resulted in better

*Electrochemical Society Member.
[z]E-mail: yanting.liu@kit.edu

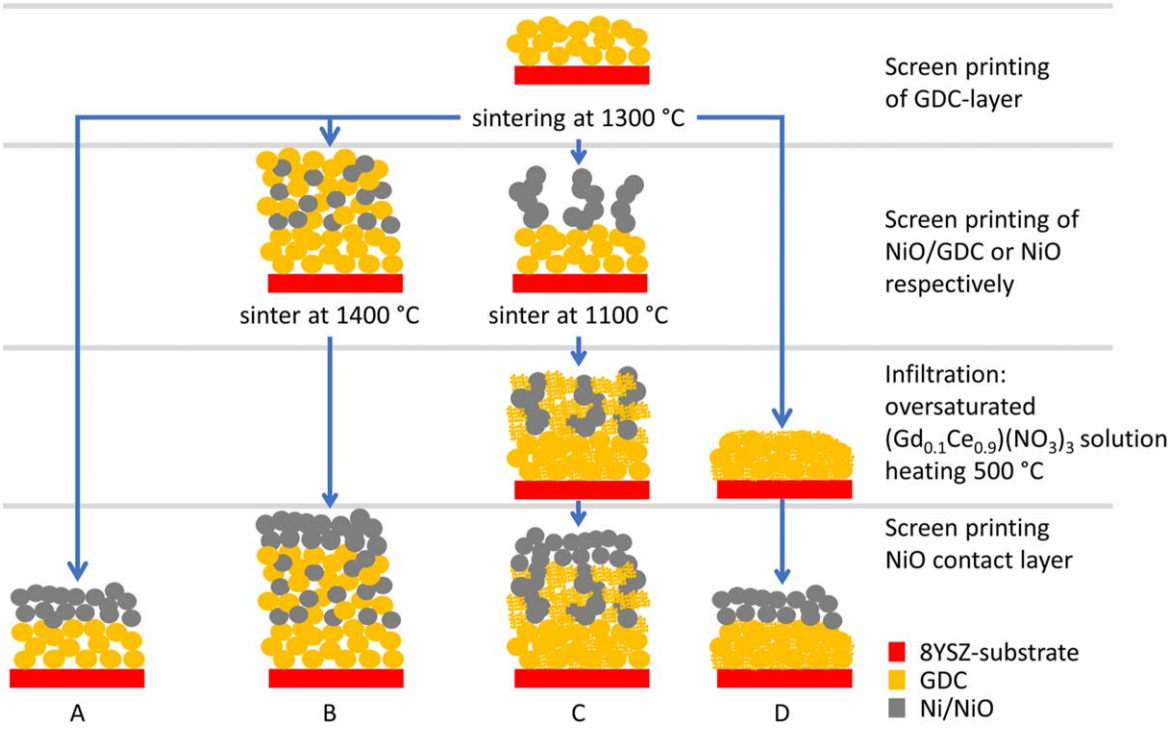

Figure 1. Manufacturing steps and schematic structure of the four different electrodes. All cells are symmetrical, so only one electrode is presented.

performance (polarization resistance decreased from 0.830 Ωcm^2 to 0.050 Ωcm^2 at 600 °C) and higher aging resistance. It was found that the fine distribution of Ni nanoparticles after infiltration into the pre-sintered YSZ or cerium dioxide-based skeleton could provide sufficient electrical conductivity in the anode despite the low content.[15–17] Infiltrating GDC into a pure Ni anode improved the polarization resistance from 10.7 Ωcm^2 to 1.50 Ωcm^2 at 700 °C.[18–20] The performance of cells resulting from the infiltration of GDC into a porous backbone of pure Ni reported in the literature[20] did not achieve as good results as those from the infiltration of Ni or Ni-ceria into metal-ceramics[14] or sintered oxide backbones.[21]

Several studies have delved into the structural changes observed in commonly utilized Ni/GDC anodes. The primary aging phenomena are attributed to Ni coarsening, agglomeration, and depletion.[22,23] Compared to the stable zirconia matrix, microstructural changes in the GDC structure were observed in Ni/GDC mixtures.[22,24,25] As particle growth occurs, the contacts between Ni-Ni and Ni-GDC gradually diminish, resulting in a decrease in TPB density and an increase in electronic resistance. Ni depletion contributes to a reduction in active reaction sites within the active part of the electrode layer. Additionally, the loss of Ni may lead to a significant increase in ohmic resistance. Another noteworthy phenomenon is the GDC coating of the Ni surface after approximately 15,000 h.[22,24] This coating not only prevents Ni coarsening but also hinders mass transport, decreasing TPB and Ni percolation. In the work of Holzer,[24] quantitative particle size evolution of Ni, pore, and GDC under different conditions is reported. The growth of all particles exhibited a temperature and humidity-strengthened effect.

In this study, we conducted a comparative analysis of symmetrical cells featuring different Ni/ceria anodes. Alongside screen-printed and sintered pure GDC and Ni/GDC electrode layers, we introduced GDC infiltration into a NiO-skeleton, a method rarely reported in other research compared to infiltrating Ni into a ceramic-oxide matrix, and explored its potential in improving electrode performance. The latter electrodes exhibited remarkable performance, achieving a polarization resistance of 0.195 Ωcm^2 at 600 °C. To evaluate the durability of this innovative GDC-infiltrated Ni-skeleton anode and study the structural evolution of nano-GDC particles, cells underwent aging at elevated temperatures of 700 °C and 900 °C. Secondary electron microscopy (SEM) analyses revealed elevated TPB and double-phase boundary (DPB) densities, facilitated by the nanoscale structure of the infiltrated GDC. The accelerated aging at temperatures significantly above the targeted operating temperature confirmed the thermal activation of cell aging. Microstructural analysis indicates that the observed increase in polarization resistance is attributable to the thermally activated sintering of the GDC phase.

Experimental

In this paper, 4 types of electrolyte supported cells (ESC) with 1 cm^2 symmetrical electrodes produced at Forschungszentrum Jülich GmbH were investigated. The manufacturing processes and schematic structures of all cell types are presented in Fig. 1.

As shown in Fig. 1, starting from an 8YSZ electrolyte substrate (200 μm; Kerafol GmbH & Co. KG, Eschenbach i. d. Opf., Germany), a GDC paste was screen-printed and sintered at 1300 °C. Based on this "inter" layer, cell A was obtained by screen-printing a NiO layer. Using the same GDC interlayer, the NiO/GDC paste was printed and sintered at 1400 °C. After printing the NiO layer, cell B was obtained. For the fabrication of Cell C, a NiO paste was first screen-printed onto the GDC interlayer and sintered at 1100 °C to form the NiO backbone. The cells were immersed in an oversaturated $(Gd_{0.1}Ce_{0.9})(NO_3)_3$ solution for 5 min, dried and calcined at 500 °C to obtain a GDC structure inside the pores of the NiO layer. This step was repeated five times to ensure an adequate amount of GDC. Finally, the NiO layer was printed. Cell D also started from a substrate with a sintered GDC interlayer, which was infiltrated according to the same procedure as Cell C but without the NiO scaffold. The NiO layer was then printed on top of the GDC-infiltrated GDC layer. The electrodes of Cells A-D are named electrode A-D, respectively. Microstructures of the electrodes after reduction and a short-term test at 600 °C(except cell D) are shown in Fig. 2. Due to the lack of sintering, the Ni contact layer showed relatively poor adhesion to the sintered parts of the electrode and delaminated during demounting the cell from the test bench. Due to

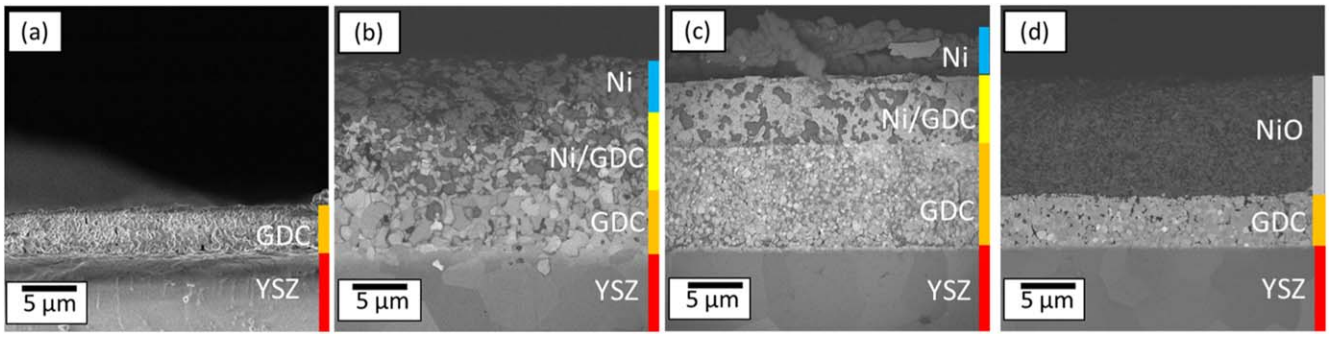

Figure 2. SEM/back scattering electron (BSE) images of the 4 types of electrodes. The electrolyte substrate is marked in red, the GDC layer in orange and the Ni contact layer on top in blue (delaminated in (a)). Cell D is unreduced and the NiO layer is marked in light grey. Cells B and C exhibit a Ni/GDC layer marked in yellow. (a) Image of fractured cell A. SEM image from mirror detector, electron energy: 3 keV, beam current: 20 nA. (b) Image of fractured cell B. (c) Image of fractured cell C. (d) Image of fractured unreduced cell D. (b-d): BSE images from an in-column detector, electron energy: 3 keV, beam current: 20 nA. In the Ni/GDC (yellow) layer, the darker grey corresponds to Ni, lighter grey to GDC.

Table I. Porosity of electrode A-D.

Electrode	Porosity [−]
A	0.44 (estimated)
B	0.38
C	0.25 (estimated)
D	0.08 (estimated)

Table II. Operating conditions of the aging test. The fuel gas composition was a hydrogen/steam-mixture of 1:1.

Cell	Temperature °C	Time h
C.1	600	0
C.2	700	1000
C.3	900	640

the delamination of the electrode layers in cell D, the microstructure of an as-produced cell in the unreduced state was analyzed in the SEM. As presented in Fig. 2, cells A, B and D have GDC interlayers with comparable thicknesses of roughly 4.8 μm while cell C has nearly double the thickness. The porosities of electrodes A-D are listed in Table I. The value for electrode B is obtained from reconstruction, while the porosities of electrodes A, C, and D are estimated using Image J / Fiji based on SEM images of the cross-section.

The cell stacking and test method are detailed in Ref. 26, and a comprehensive description of the test bench is available in Ref. 27. Four cells of types A-D were assembled between two side cells (bottom and top) from cell B and gradually heated in a N_2 (95%)/H_2 (5%) mixture at a heating rate of 1 K min^{-1} until reaching 650 °C. The gas composition was then changed to N_2 (65%): H_2 (30%): H_2O (5%) and maintained for 6 h. After adjusting the gas composition to hydrogen (0.500 slm) and oxygen (0.125 slm) to create a hydrogen/steam mixture of 1:1, cells were characterized by electrochemical impedance spectroscopy (EIS) at 650 and 600 °C. Following this initial characterization, the furnace was cooled down in nitrogen (90%) and hydrogen (10%), maintaining a total flow rate of 0.500 slm throughout the process.

Two type C cells underwent additional heating for accelerated aging tests. One cell, labeled C.1, was only reduced and not exposed to additional high-temperature heating. The remaining cells, labeled C.2 and C.3, were subjected to additional high-temperature treatments under conditions detailed in Table II. During aging, reference impedance measurements at 600 °C were conducted on both cells every few hundred hours. After the polarization resistance of cell C.3 reached a plateau, a comprehensive characterization, involving multi-parameter variations similar to,[13] was carried out, allowing the aging during characterization to be neglected. Additionally, an inert gas alternating test was performed on cell C.2 to investigate gas diffusion loss.

All impedance measurements were conducted under open-circuit voltage (OCV) conditions to ensure electrochemical symmetry across both electrodes. As indicated in Ref. 28, high-frequency processes (HF, >10 kHz) are associated with the resistance within the electrolyte and the GDC/YSZ interface. Consequently, the real value at 10 kHz is designated as the ohmic resistance. The difference between this value and the maximum on the real axis represents the polarization resistance. Throughout this study, all spectra and their corresponding Distribution of Relaxation Times (DRTs) are plotted within the 10 kHz frequency range.

Following the tests, all cells were disassembled and prepared for SEM analysis using a Thermo ScientificTM Helios G4FX DualBeamTM (Thermo Fisher Scientific, Waltham, Massachusetts, USA). In Figs. 4–6 and 14, all BSE images were captured with an in-column detector, employing an electron energy of 3 keV, a beam current of 20 nA, and a tilt angle of 52°. Energy-dispersive X-ray (EDS) analyses (XFlash Detector 5030, Bruker AXS, Karlsruhe, Germany) were conducted on cells A and B in the GDC layers. To investigate the cause of the extra-thick GDC interlayer in cell C, another Cell C.4 was fractured and analyzed with SEM without reduction.

Results and Discussion

Initial performance and microstructure of the different cell types.—In Fig. 3, impedance spectra measured initially at 600 °C (50% H_2 + 50% H_2O) and the related DRTs for one electrode of each cell are presented. All impedance spectra and corresponding DRTs shown in this work are halved from the spectra of the cell for single electrode evaluation. The identification of the processes based on electrode C is detailed later in this work.

Electrode A unexpectedly reached an acceptable performance with a polarization resistance of 0.260 Ωcm^2 (2 cells tested, average: 0.269 Ωcm^2, relative standard deviation (RSD): 2.56%). The reason behind this is most probably an interdiffusion of Ni from the contact layer into the porous GDC layer,[29] enhancing the electrochemical activity of the GDC surfaces. An EDS analysis in the GDC layer showed a Ni content of 1.87 at%. The DPB (GDC-pore) seems to be activated by this Ni. Besides, the thin overlapping area where GDC is in direct contact with the Ni-contact layer may also contribute to the electrochemical reaction.

Although the pure GDC sample in Ref. 30 exhibits a comparable microstructure and also employs a Ni current collector, its measured polarization resistance of 2.00 Ωcm^2 is seven times larger than that

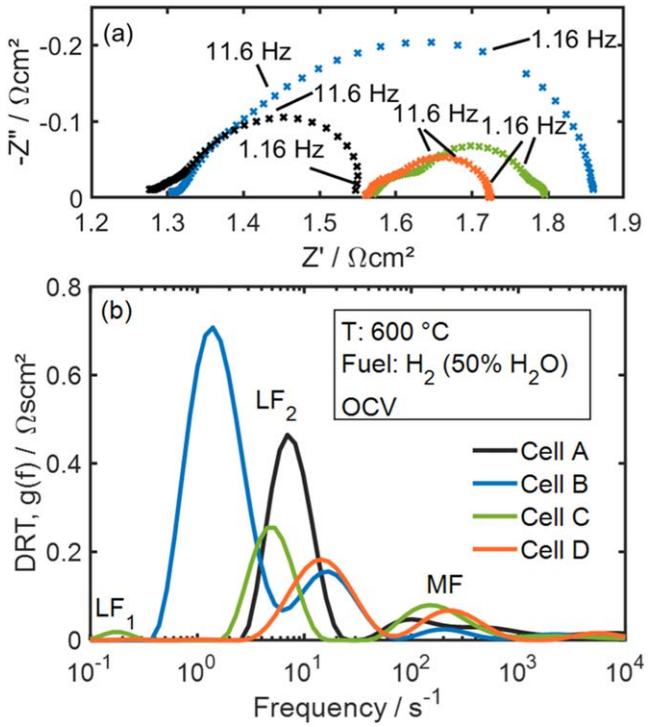

Figure 3. Impedance spectra of (a) electrode A-C, (b) electrode D and (c) corresponding DRTs measured initially at 600 °C (50% H_2 + 50% H_2O). The values are halved from the spectra of the cell for single electrode evaluation.

of electrode A. This disparity could potentially originate from differences in the GDC powder and reduction process. In another study by our group[29] utilizing the same GDC powder as electrode A, a polarization resistance of approximately 0.210 Ωcm^2 was achieved at 600 °C (70% H_2 + 30% H_2O). The slight variance in polarization resistance could be attributed to the lower sintering temperature of 1100 °C, resulting in a finer GDC structure.

Compared to electrode A, electrode B, consisting of 38% pores, 22% Ni, and 40% GDC, exhibited approximately twice the polarization resistance, measuring 0.547 Ωcm^2 (based on 5 tested cells, with an average of 0.584 Ωcm^2 and RSD of 4.42%). The DRT plot, depicted in blue, reveals an enlargement and shift towards low frequency of both peaks within the 1–400 Hz range. Since the low-frequency peak primarily corresponds to electrochemical reactions

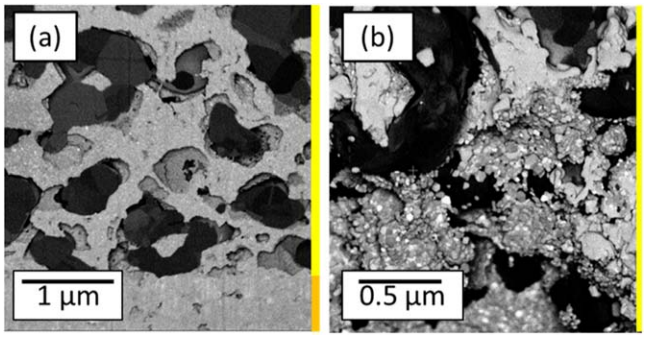

Figure 5. BSE images of FIB-polished (a) and unpolished (b) cross-section of electrode C (C.1) after reduction and short-term test at 600 °C. The GDC layer is marked in orange, and the Ni/GDC layer in yellow. The darker grey corresponds to Ni, lighter grey to GDC.

(as noted in Ref. 28), this increase likely indicates a reduction in active reaction sites.

The microstructure comparison (as shown in Fig. 4b) reveals a much coarser GDC layer in sample B, attributed to the second sintering procedure of the Ni/GDC layer at an even higher temperature of 1400 °C. Assuming electrochemically active GDC surfaces activated by Ni (4.85 at. % Ni according to the EDS analysis) diffused into this nominally pure GDC layer, the reduced volume-specific surface area might have increased the polarization resistance. The potentially larger amount of Ni in this layer appears to be of minor importance. Further investigations are required to analyze the impact of DPB density, nickel amount, and spatial distribution on the performance of such GDC layers.

In any case, the Ni/GDC layer, originally intended to be the electrochemically active electrode, seems to exhibit a subordinate impact on the performance. Considering a transmission line behavior extending over the two layers[31] and a typical penetration depth of a few micrometers only,[30] it is reasonable that the Ni/GDC layer hardly provides any electrochemical performance but limits gas transport, as well as increases the ohmic resistance of cell B. The latter is due to the non-percolating Ni in this layer enforcing electronic transport in the GDC phase.

For electrode C, consisting of approximately 25% pores, 30% Ni, and 45% GDC, a polarization resistance below 0.20 Ωcm^2 is achieved (3 cells tested, average: 0.205 Ωcm^2, RSD: 5.27%). In this electrode, an extremely fine GDC microstructure resulting in a high DPB density and still sufficient porosity due to the reduction of the NiO backbone are achieved (Fig. 5). The latter was analyzed

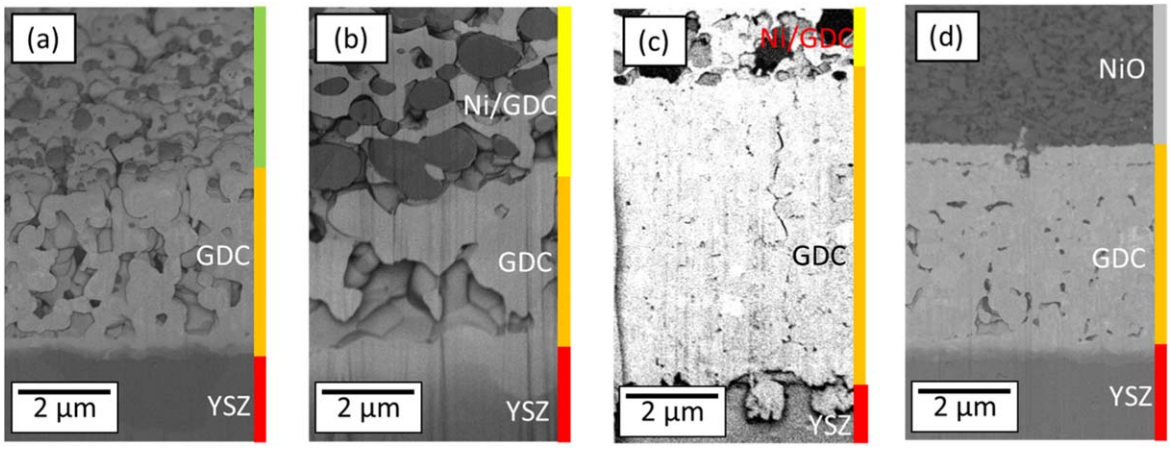

Figure 4. BSE images of FIB-polished cross sections of reduced cells A (a), B (b), C (mostly in GDC interlayer) (c) and unreduced cell D (d). The 8YSZ electrolyte is marked in red, the GDC layer in orange, the Ni/GDC layer in yellow and NiO contact layer in light grey. The area marked in green in (a) is the top view of the GDC layer visible due to a tilt angle of 52°.

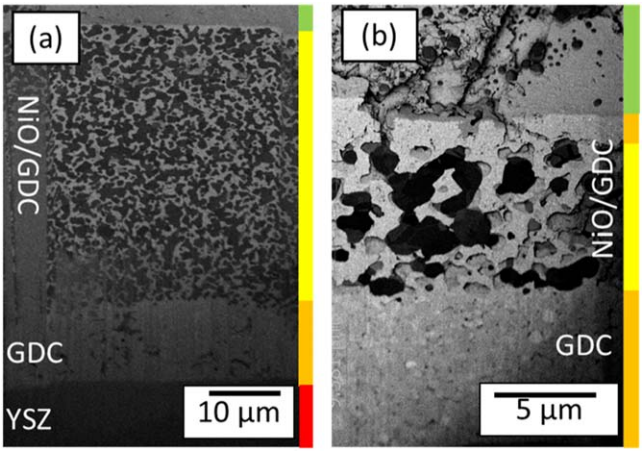

Figure 6. BSE images of FIB-polished (a) cross-section of electrode C (C.4) before reduction and (b) electrode C (C.1) after reduction. The GDC layer is marked in orange, the Ni (NiO)/GDC layer in yellow, YSZ in red and the top view in green. The darker grey corresponds to Ni/NiO, and the lighter grey to GDC in the Ni/GDC layer.

using inert gas changes as described in Ref. 13, proving that the gas diffusion resistance at 600 °C is estimated to be below 1×10^{-5} Ωcm^2. Due to the presence of the Ni backbone, activation of the rather large GDC surfaces as well as a high density of TPBs is reasonable.

Cell C exhibits a larger ohmic resistance of 0.250 Ωcm^2 compared to cells A and B, despite having a denser GDC interlayer, which should result in higher effective ionic conductivity. This disparity may be attributed to the thicker GDC interlayer and the additional uneven GDC layer atop electrode C.1, as illustrated in Fig. 6b. Based on measurements of ionic and electronic conductivity under the same conditions in Ref. 29, the additional 5 μm thick GDC interlayer (as ionic conductor) and 2 μm thick GDC layer (as electronic conductor) atop the electrode contribute approximately 0.150 Ωcm^2 of ohmic resistance, assuming a tortuosity of 1. Deterioration of contact due to wet infiltration is also a potential contributing factor.

The SEM images of the cross-section of cell C, before and after reduction (Fig. 6), indicate that the GDC interlayer was approximately 5 μm thick before reduction, similar to other cells. The NiO/GDC layer measured about 20 μm in thickness and comprised NiO particles around or smaller than 0.50 μm. After reduction, as shown in Fig. 6b, the Ni/GDC layer was approximately 6.5 μm thick, which is 13.5 μm thinner than before. Simultaneously, the GDC interlayer increased to 9.5 μm. An additional GDC layer on top of the Ni/GDC electrode, under the Ni-contact layer with uneven thickness (~2 μm), was also observed. These observations suggest a dynamic electrode reorganization during reduction.

The significant increase in Ni particle size (from approximately 0.5 μm to 1 μm, a 100% increase) after reduction suggests that during this process, Ni/NiO migrated towards the center of the NiO/GDC layer and underwent reduction, resulting in the formation of larger Ni particles. Consequently, both edges of the original electrode layer (20 μm) became devoid of Ni particles. The lower portion of the NiO/GDC layer likely contributed to the increased thickness of the GDC interlayer, while the upper portion formed an additional GDC layer beneath the Ni current collector, which exhibits inferior electron conductivity. Further investigation of this phenomenon would be an additional test employing a camera to record the cross-section of electrode C during reduction. Unfortunately, this is not currently feasible at our institute due to hardware limitations. Despite the potential presence of Ni particles within the GDC layers, the dense nature of the entire GDC layer, as depicted in Fig. 4c, impedes gas diffusion. Therefore, while the GDC

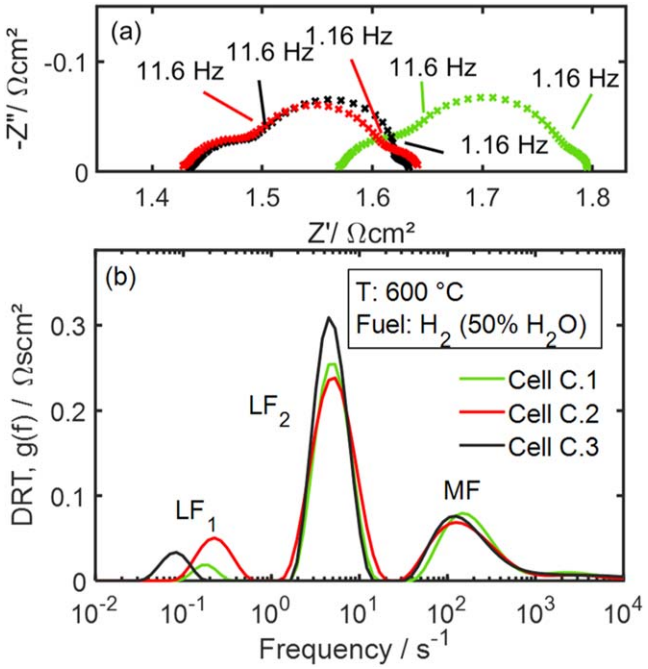

Figure 7. (a) Impedance spectra and (b) corresponding DRTs of electrodes of 3 cells of type C measured initially at 600 °C (50% H_2 + 50% H_2O).

layer might primarily contribute to ohmic resistance, its impact on electrode performance is not considered significant.

Infusing fine GDC particles into a Ni-skeleton is feasible to obtain a polarization resistance as low as 0.195 Ωcm^2 at 600 °C. Notably, electrode C surpasses values reported in Ref. 18 by at least 10-fold, highlighting the method's greater potential than initially anticipated. Even when compared to electrodes featuring high GDC composition, such as those incorporating nano-Ni particles on the GDC surface,[30] electrode C remains competitive. However, in comparison to the optimal results reported in the literature[21] for electrodes obtained by infiltrating Ni into the GDC matrix, electrode C falls short in terms of performance.

Three Cell Ds were characterized, but poor reproducibility was observed. The acquired ohmic resistances for half-cells were 6.00, 1.48, and 1.55 Ωcm^2, respectively. Correspondingly, the polarization resistances for one electrode were 1.20, 0.245, and 0.164 Ωcm^2. We will exclude the first cell from further discussion due to its poor quality and deterioration during fabrication. While the other two cells had similar ohmic resistances, their electrode performance differed significantly, making a comparison to other electrodes impractical. In this study, the impedance and corresponding DRT of the best-performing electrode D are presented in Fig. 3. However, due to electrode delamination, SEM analysis to understand the reasons behind its good performance was not possible. It is assumed that the infiltration of GDC into the GDC-skeleton was not fully successful in filling all pores, as observed in the fourth unreduced electrode D (Fig. 4d). Therefore, no definitive conclusions can be drawn regarding its superiority or inferiority compared to other electrode types. The additional heating treatment of Cell C (1100 °C after printing NiO paste) may have contributed to its lower frequency in delamination and higher stability in performance.

Characterization of cell C.—The nanoscale microstructure of the infiltrated GDC, which was only annealed at 500 °C, raises questions concerning stability at nominal operating conditions. Three cells were tested for different durations at various temperatures to investigate stability. Figure 7 shows the impedance spectra and corresponding DRTs measured initially at 600 °C for one electrode

of the three cells. Only minor deviations in ohmic and polarization resistance were observed. The ohmic resistances of the three tested cells are 1.570, 1.428, and 1.434 Ωcm^2 (halved values), respectively. The differences could be partly related to unmatured manufacturing procedures, and the randomness of possible electrode reorganization during reduction. The electrodes also reached quite similar polarization resistance values of 0.220, 0.195, and 0.200 Ωcm^2 at 600 °C (50% H_2 + 50% H_2O). The DRTs show some differences in the small peak LF_1 below 1 Hz, but the peak LF_2 around 6 Hz and the peak MF around 150 Hz are in good agreement. The first is proved to be sensitive to alternating inert gas types during ending characterization on cell C.2 (Fig. 8d). Thus, this peak is possibly related to gas diffusion loss.[13] Considering this, a quite similar initial microstructure of all samples can be assumed, and the microstructural differences revealed in post-test analyses can be attributed to microstructural changes that occurred during testing.

To isolate degradation related only to the electrode, characterization involving multi-parameter variation was performed on cell C.3. The EIS measurements were carried out analogous to operating conditions in Ref. 28. All measurements were recorded at OCV with a total gas flow rate of 0.500 slm in this work.

Figure 8 shows DRTs of measured impedance spectra of the electrode of cell C.3 at temperatures between 845 to 900 °C under different gas compositions and the electrode of cell C.2 at 700 °C with alternating inert gas. Compared to the two main contributions reported in Refs. 13 and 28 more processes with non-negligible contributions were observed. The 4 visible peaks at 845 °C are named LF_1, LF_2, MF_1 and MF_2 from low to high frequencies. It seems that at higher temperatures and/or lower steam content, the process between 30–1000 Hz in Fig. 7 is separated to be 2 middle-frequency processes, MF_1 and MF_2. According to,[28] high-frequency processes (HF > 10000 Hz at 845 °C) correspond to the resistance within the electrolyte and the GDC/YSZ-interface and thus are not part of the interest of this work and will not be discussed further.

Figure 8a shows that all processes except LF_1 are thermally activated. As stated in Ref. 28, they can be attributed to charge transport and/or charge transfer processes. The second middle-frequency process reported to appear at a lower temperature in Ref. 28 is not comparable in terms of either temperature dependency or value to the MF_2 observed in our cell. Thus, it is probably not neglectable and addressing its origin could be important for degradation analysis. The temperature dependency of process LF_1 is weak, suggesting a possible association with the gas diffusion process.

To investigate the dependence of the electrode processes on fuel humidification, the steam content was varied between 0.05 and 0.50 atm at a constant hydrogen partial pressure of 0.3 atm and temperature of 845 °C. A relatively high operating temperature was chosen to suppress an overlap of MF_1 and MF_2. The DRTs of impedance spectra shown in Fig. 8b show that the process LF_1 has the strongest dependency on steam content followed by LF_2. Increasing steam partial pressure significantly decreases their contributions to polarization resistance. The process MF_1 has relatively weaker dependency in analog to that reported in Ref. 28, and could be attributed to oxide ion transport in the GDC phase of the electrode. With increasing steam content resulting in higher oxygen partial pressure, the decrease of ionic conductivity of GDC[32] should be partly responsible for the increase in MF_1. In comparison, the process MF_2 showed nearly negligible dependency on water steam partial pressure.

Similar investigations were carried out regarding the impact of hydrogen partial pressure. Compared to varying steam content, all processes show weaker dependency (Fig. 8c). Among all processes, LF_1 is the most sensitive to hydrogen content, followed by

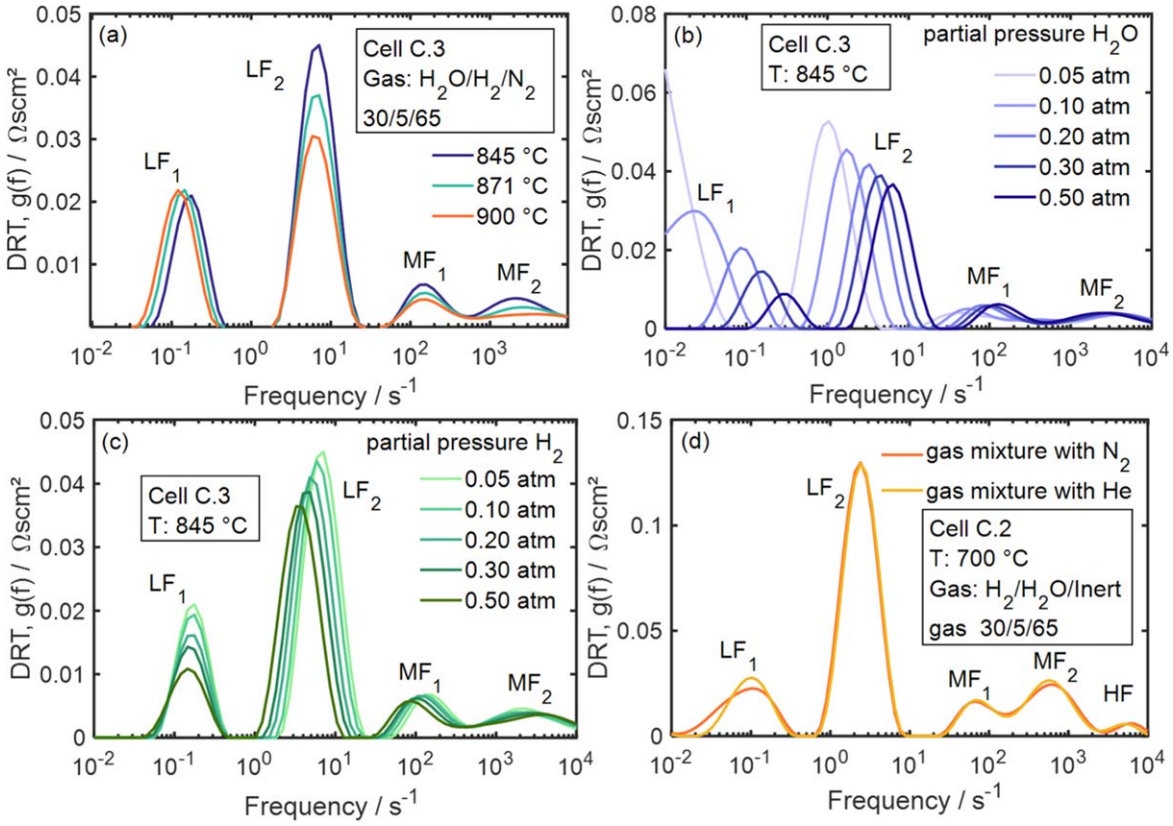

Figure 8. DRTs of impedance spectra of the electrode of cell C.3 (a) at different temperatures between 845 °C–900 °C, steam and hydrogen partial pressures are 0.05 and 0.30 atm with nitrogen as inert gas, (b) at 845 °C when changing steam partial pressure from 0.05 to 0.50 atm, while keeping hydrogen partial pressure constant to be 0.30 atm with nitrogen as inert gas, (c) at 845 °C when changing hydrogen partial pressure from 0.05 to 0.5 atm, while keeping steam partial pressure constant to be 0.30 atm with nitrogen as inert gas. (d) DRTs of impedance spectra of the electrode of cell C.2 under different inert gases (steam and hydrogen partial pressures are 0.05 and 0.30 atm at 700 °C).

LF_2. With an increasing hydrogen partial pressure, both low frequency processes' contribution to polarization resistance decreases. The process MF_1 is weakly dependent, possibly due to the ionic and electronic conductivity of GDC depending on the oxygen partial pressure. The dependence of process MF_2 on hydrogen partial pressure seems to be weak. However, due to its small value and strong overlapping, a precise description of its behavior is not possible.

A test where inert gas was altered analogously to the procedure reported in Ref. 13 on cell C.2 was performed. Since hydrogen and steam have different diffusion velocities in nitrogen, and helium and they are both electrochemically inert, only gas diffusion-related processes would be influenced.[33] As shown in Fig. 8d, process LF_1 shows clear dependency on alternating inert gas, leading to a difference of 5.00 $m\Omega cm^2$ in polarization resistance under the given gas mixture. Compared to the value reported in Ref. 13, this value is nearly 3 times smaller. It is partly due to lower testing temperature and a different gas composition, but it should also be partly due to the application of active driven gas layer concept described in Ref. 26. The different geometry might account for the lower feature frequency of the gas diffusion process (~0.1 Hz at 845 °C) despite its smaller value compared to that in Ref. 13. In contrast, processes LF_2 and MF_1 are not influenced. They are not related to the gas diffusion process. A small change of process MF_2 in Fig. 8d was observed. However, after a complex nonlinear least square (CNLS)-fit with a RQ-element for MF_2, the change in its resistance is only 0.50 $m\Omega cm^2$, which is 10% of the resistance difference in process LF_1 induced by exchanging inert gas. Thus, this is more likely to be measurement deviations.

Till this step, we identified and correlated 2 low-frequency and one middle-frequency processes LF_1, LF_2 and MF_1 to a gas diffusion, a surface and a bulk process, respectively. Suggestions for their origin can be referred to in Ref. 28. However, the origin of another middle-frequency process MF_2 is still unknown. Because the two middle-frequency processes are not separable at 600 °C where reference impedances were measured, the degradation analysis would be mainly based on the evolution of low-frequency process LF_2.

Aging test of cell C.—In Fig. 9, all times presented in legends are system times. The first reference impedance recorded at 600 °C for Cell C.2 was 40 h after the start of the test. In between, heating up, reduction of the cell, and gas composition adjustment were performed. After that, it took another 10 h to set the operating condition at an elevated temperature of 700 °C. The same applies to Figs. 10–12.

During 1000 h of operation at 700 °C, the ohmic resistance showed an increase (Fig. 10a), which is at least partly due to intrinsic conductivity degradation of zirconia electrolyte.[34] Another possibility could be the agglomeration of Ni particles in the Ni contact layer accompanied by a contact loss. The gas diffusion peak LF_1 has decreased between 50 and 250 h (Fig. 10b), possibly due to fine GDC particle coarsening, resulting in enlarged pores (Figs. 14a, 14b). Surface process LF_2 showed minor enlargement along the timeline while middle frequency peaks increased stronger. Due to the strong overlapping between MF_1 and MF_2, concluding whether degradation took place in either or both processes is impossible.

The reference measurements performed at 600 °C showed similar results for ohmic resistance, LF_1 and LF_2 processes, as presented in Fig. 9. Two middle frequency processes overlap to be one peak in DRT (Fig. 9b), where the most increase in polarization resistance took place. As stated above, whether degradation of middle frequency processes occurred in electrode is unknown. With the evolution of LF_2 as an indicator of electrode degradation, only minor changes in electrode of cell C.2 are expected.

As presented in Fig. 11, the evolution of impedance spectra of the electrode C.3 during operation at 900 °C is different from electrode C.2 at 700 °C, apart from a continuous increase in ohmic resistance (Fig. 11a). The gas diffusion process LF_1 increased between 49 and 73 h

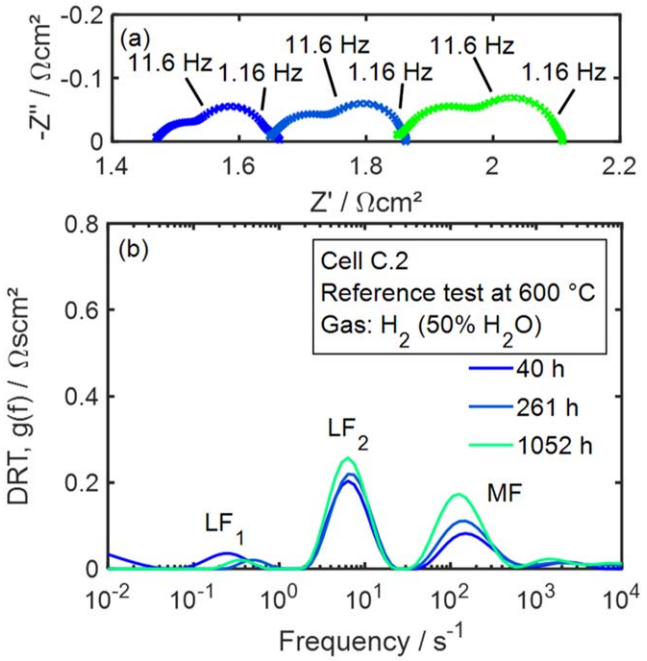

Figure 9. Time evolution of (a) impedance spectra and (b) corresponding DRTs of the electrode of cell C.2 measured at 600 °C under a gas mixture of steam: hydrogen 50: 50 for reference.

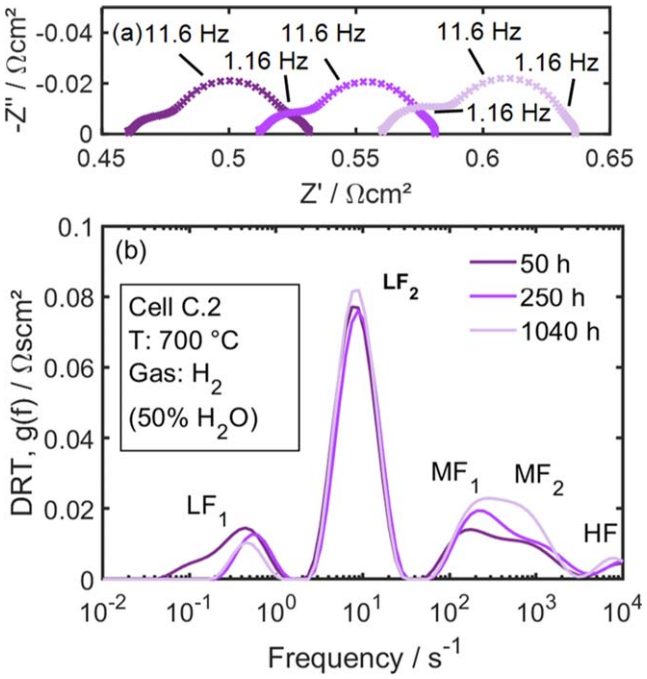

Figure 10. Time evolution of (a) impedance spectra and (b) corresponding DRTs of the electrode of cell C.2 operated at 700 °C under a gas mixture of steam: hydrogen 50: 50.

(Fig. 11b). A possible explanation could be pore closing due to drastic GDC phase structural change caused by high temperature, such as possible densification in the extra GDC layer on top of Ni/GDC electrode. Afterwards, the gas diffusion loss showed a decrease similar to that shown in Fig. 10b. Peak MF_1 increased with operating time. MF_2 also increased slightly. The contribution of process LF_2 at 900 °C to polarization resistance increased first (area under LF_2 peak at 73 h larger than at 49 h in DRT), followed by a continuous decrease observed until 673 h. At the end of the test, the contribution of process LF_2 is smaller

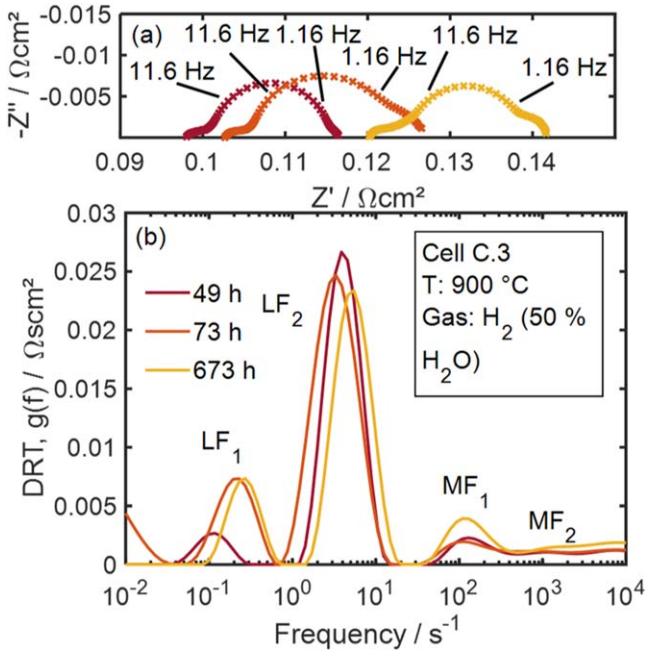

Figure 11. Time evolution of (a) impedance spectra and (b) corresponding DRTs of the electrode of cell C.3 operated at 900 °C under a gas mixture of steam: hydrogen 50: 50.

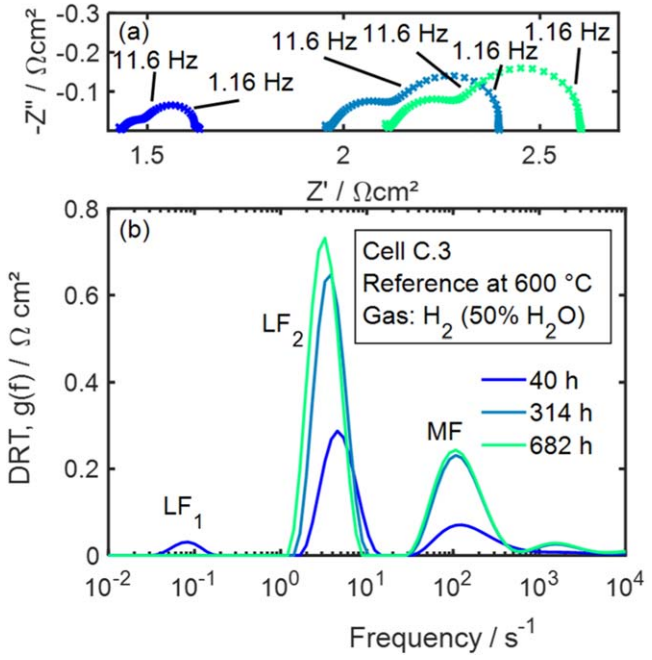

Figure 12. Time evolution of (a) impedance spectra and (b) corresponding DRTs of the electrode of cell C.3 measured at 600 °C under a gas mixture of steam: hydrogen 50: 50 for reference.

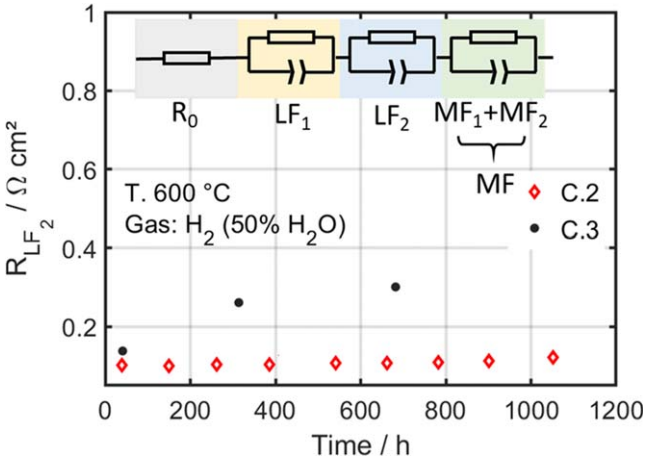

Figure 13. Time evolution of fitted value of process LF_2 of the electrode of cell C.2 and C.3 measured at 600 °C under a gas mixture of steam: hydrogen 50: 50 for reference.

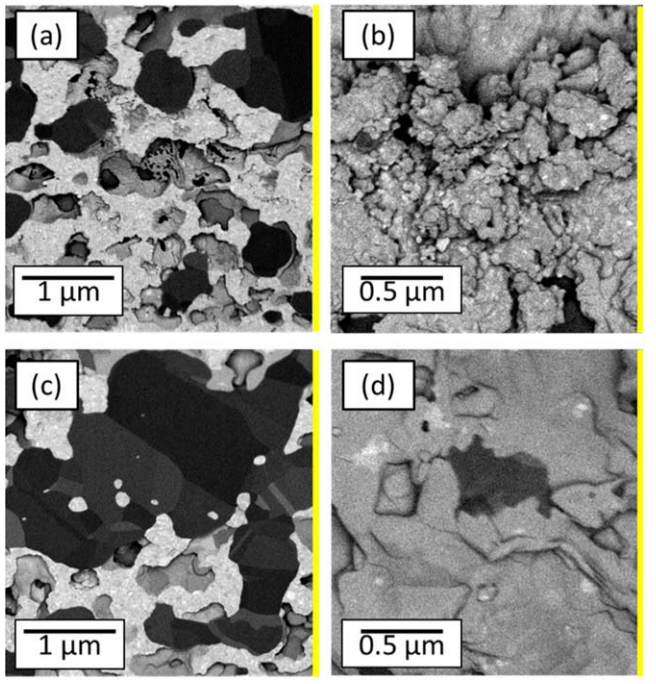

Figure 14. BSE images of polished (a) and un-polished (b) cross section of the Ni/GDC layer in cell C.2 after operating at 700 °C for 1000 h and BSE images of polished (c) and un-polished (d) cross section of the Ni/GDC layer in cell C.3 after operating at 900 °C for 640 h. The darker grey corresponds to Ni, lighter grey to GDC.

than its initial value. The increase in LF_2 could be explained by electrode degradation, possibly due to Ni agglomeration, GDC particle coarsening, and the resulting losses in TPB and DPB (Figs. 14c, 14d). No clear explanation could be found for the long-term decrease of LF_2 between 73 and 673 h. A similar "improvement" was observed in former research of our group[26] and attributed to possible activation of porous GDC interlayer by diffusion of nano nickel particles. However, due to the dense GDC interlayer (Fig. 4c) in cell C probably prohibiting the diffusion of nickel into it, such an assumption is not sufficient. Further investigations are necessary to fully explain the changes in impedance.

Based on the complex impedances recorded at 900 °C, it is assumed that very complicated and/or time-dependent inhomogeneous structural changes might have taken place inside the electrode, which are not supposed to be seen at the nominal operating temperature (600 °C).

Reference measurements performed at 600 °C presented in Fig. 12 show clear thermally activated aging in both ohmic resistance and process LF_2. Due to the lack of data at around 73 h, it is not clear if improvement in peak LF_2 is also visible at 600 °C. But overall, the contribution of this process to polarization resistance at 600 °C has increased largely after operating at 900 °C for around 650 h. Further investigations are needed for the discrepancy in the evolution of process LF_2 at 900 and 600 °C. The discrepancy in the evolution of process LF_1 might be due to a small peak shift towards higher frequency, leading to stronger overlap and the weak

temperature-dependent LF_1 being less prominent, resulting in an invisible peak after the calculation of DRT at a lower temperature.

Based on the characterization and accelerated aging test results, an equivalent circuit model for CNLS-fit displayed in Fig. 13 is obtained for half of the cell. It consists of an ohmic resistance R_0, and 3 resistances parallel to a constant-phase-element (R||CPE). They are used to fit LF_1, LF_2, and middle frequency processes MF_1+MF_2. One R||CPE is applied to fit MF_1 and MF_2 since they are not separable at 600 °C in a gas mixture of steam: hydrogen 50:50. The gas diffusion, middle and high frequency processes are not further considered under the frame of this work. To enable a direct comparison of tested cells, the fitted values of process LF_2 at 600 °C are presented in Fig. 13. The contribution of LF_2 to polarization resistance increased from 0.102 to 0.121 Ω cm^2, corresponding to an 18.6% increase when operated at 700 °C within 1000 h. In contrast, this value for C.3 has increased from 0.137 to 0.301 Ω cm^2, indicating an 120% increase. Compared to electrode C.2, electrode C.3 aged 5 times faster within a shorter time, suggesting a thermally activated degradation mechanism.

Post-test analysis of cell C.—Figures 5 and 14 depict the BSE images of tested cells C.1, C.2, and C.3. It's evident that the first two cells, C.1 and C.2, exhibit similar Ni tomography after the test, with GDC particles experiencing coarsening during testing at 700 °C but remaining in the range of 50 nm, maintaining high densities of TPB and DPB. However, at the elevated temperature of 900 °C, a different phenomenon was observed in cell C.3. As illustrated in Figs. 14c, 14d, the sintering effect of the elevated temperature is apparent, with both the nanoscale GDC and Ni frameworks experiencing particle coarsening. In comparison to the results reported in Ref. 24, the growth of GDC is more evident and pronounced than that of Ni particles. GDC phase coating of Ni surfaces occurred within less than 700 h. No Ni depletion was witnessed, likely due to operation under OCV without polarization. The resulting decrease in DPB and TPB density is most likely responsible for the observed increase in polarization resistance.

Conclusions

The electrochemical and microstructural analysis of four types of nickel/ceria fuel electrodes, differing in layer sequences and processing parameters of the individual layers, revealed partly unexpected results. Electrode C, produced with GDC infiltrated into a pure NiO-skeleton, achieved the best stable performance with a polarization resistance of 0.195 Ωcm^2 at 600 °C.

Fuel electrode A, consisting of a sintered GDC layer (1300 °C) contacted by a non-sintered Ni layer, exhibited rather high performance. The low polarization resistance of only 260 mΩcm^2 at 600 °C was attributed to minor amounts of Ni (1.85 at. %) diffused into the GDC layer. Thus, the GDC layer, intended to be used as an interlayer between the 8YSZ-electrolyte and a Ni/GDC electrode, acts as a mixed ionic-electronic conducting electrode with DPBs activated by Ni. It is noteworthy that careful in-depth cell characterization is necessary, as even a simple contact layer introduced to better contact the electrode to the current collector mesh can drastically influence performance.

In the case of cell B, exhibiting an additional Ni/GDC electrode layer between the GDC layer and Ni contact layer, approximately twice as high polarization resistance was observed, most probably related to the additional sintering step for the Ni/GDC electrode layer at 1400 °C. This resulted in significant densification and particle growth in the GDC layer, decreasing its DPB density and thus the performance of electrode B.

In the case of cell C, a Ni/GDC electrode layer was produced via infiltration of GDC into a NiO-skeleton on top of a GDC layer. Possible drastic structural changes during reduction process might have led to inevitable increase in GDC thickness at both sides of Ni/GDC layer. This approach could achieve polarization resistance values as low as 195 mΩcm^2 at 600 °C. As pores in the GDC interlayer, which significantly contributed to the performance of electrodes A and B, were filled with GDC after infiltration, the high performance has to be attributed to the GDC-infiltrated Ni layer. Due to the nanoscaled GDC structure, this layer showed a high TPB as well as DPB density. Accelerated degradation tests at elevated temperatures (700 / 900 °C) revealed significant performance degradation, attributed to coarsening of the initially nanoscaled GDC structure by post-*mortem* SEM analysis. Very complicated structural changes might have taken place when operated at 900 °C, leading to rearrangement of the whole electrode. This should be avoided when designing accelerated aging tests. Further tests will study the durability at the nominal operating temperature of 600 °C and the impact of different fuel compositions. Besides, the test of full cells containing such anode is considered to investigate the degradation under the actual operating conditions (galvanostatic/potentiostatic operation).

Fuel electrode D, intended to be a dense GDC layer working as a fuel electrode, exhibited diverse performances and poor mechanical stability. It is assumed that the extra step of sintering at 1100 °C of cell C might stabilize the sample. The manufacturing method needs to be optimized.

Acknowledgments

The authors gratefully acknowledge funding from the Federal Ministry of Education and Research via the "WirLebenSOFC" project (BMBF 03SF0622 E and B).

ORCID

Y. Liu https://orcid.org/0000-0001-5333-8927
N. H. Menzler https://orcid.org/0000-0001-7091-0980
A. Weber https://orcid.org/0000-0003-1744-3732

References

1. B. C. Steele and A. Heinzel, *Nature*, **414**, 345 (2001).
2. C. Xia and M. Liu, *Solid State Ionics*, **144**, 249 (2001).
3. A. J. Samson, M. Søgaard, and P. V. Hendriksen, *Electrochim. Acta*, **229**, 73 (2017).
4. J. Zhang, C. Lenser, N. H. Menzler, and O. Guillon, *Solid State Ionics*, **344**, 115138 (2020).
5. Y. Matsuzaki and I. Yasuda, *Solid State Ionics*, **132**, 261 (2000).
6. K. Föger and K. Ahmed, *J. Phys. Chem. B*, **109**, 2149 (2005).
7. A. Kromp, S. Dierickx, A. Leonide, A. Weber, and E. Ivers-Tiffée, *J. Electrochem. Soc.*, **159**, B597 (2012).
8. A. Weber, S. Dierickx, A. Kromp, and E. Ivers-Tiffée, *Fuel Cells*, **13**, 487 (2013).
9. A. Weber, S. Dierickx, N. Russner, and E. Ivers-Tiffée, *ECS Trans.*, **77**, 141 (2017).
10. C. Zhang et al., *Nat. Mater.*, **9**, 944 (2010).
11. W. C. Chueh, Y. Hao, W. Jung, and S. M. Haile, *Nat. Mater.*, **11**, 155 (2012).
12. W. C. Chueh and S. M. Haile, *Phys. Chem. Chem. Phys.*, **11**, 8144 (2009).
13. C. Grosselindemann, N. Russner, S. Dierickx, F. Wankmüller, and A. Weber, *J. Electrochem. Soc.*, **168**, 124506 (2021).
14. T. B. Mitchell-Williams, R. I. Tomov, S. A. Saadabadi, M. Krauz, P. V. Aravind, B. A. Glowacki, and R. V. Kumar, *Mater. Renew. Sustain. Energy*, **6**, 1 (2017) .
15. P. Jasinski, T. Suzuki, V. Petrovsky, and H. U. Anderson, *Electrochem. Solid-State Lett.*, **8**, A219 (2005).
16. J. Qiao, K. Sun, N. Zhang, B. Sun, J. Kong, and D. Zhou, *J. Power Sources*, **169**, 253 (2007).
17. Y. Okawa and Y. Hirata, *J. Eur. Ceram. Soc.*, **25**, 473 (2005).
18. S. P. Jiang, S. Zhang, Y. D. Zhen, and W. Wang, *J. Am. Ceram. Soc.*, **88**, 1779 (2005).
19. S. P. Jiang, W. Wang, and Y. D. Zhen, *J. Power Sources*, **147**, 1 (2005).
20. S. P. Jiang, S. Zhang, Y. D. Zhen, and A. P. Koh, *Electrochem. Solid-State Lett.*, **7**, A282 (2004).
21. L. Guesnet, G. Aubert, S. Hubert, P. M. Geffroy, C. Aymonier, and J. M. Bassat, *Sustainable Energy Fuels*, **6**, 1801 (2022).
22. A. Zekri, M. Knipper, J. Parisi, and T. Plaggenborg, *Phys. Chem. Chem. Phys.*, **19**, 13767 (2017).
23. M. Trini, A. Hauch, S. De Angelis, X. Tong, P. V. Hendriksen, and M. Chen, *J. Power Sources*, **450**, 227599 (2020).
24. L. Holzer et al., *J. Power Sources*, **196**, 1279 (2011).
25. A. Nakajo, A. P. Cocco, M. B. Degostin, P. Burdet, A. A. Peracchio, B. N. Cassenti, M. Cantoni, J. Van herle, and W. K.-S. Chiu, *ECS Trans.*, **78**, 3205 (2017).
26. Y. Liu, F. Wankmüller, T. P. Lehnert, M. Juckel, N. H. Menzler, and A. Weber, *Fuel Cells*, **23**, 430 (2023) .
27. D. Klotz, A. Weber, and E. Ivers-Tiffée, *Electrochim. Acta*, **227**, 110 (2017).
28. M. Riegraf, R. Costa, G. Schiller, K. A. Friedrich, S. Dierickx, and A. Weber, *J. Electrochem. Soc.*, **166**, F865 (2019).

29. F. Kullmann, M. Mueller, A. Lindner, S. Dierickx, E. Mueller, and A. Weber, *J. Power Sources*, **587**, 233706 (2023).
30. A. Sciazko, Y. Komatsu, T. Shimura, Y. Sunada, and N. Shikazono, *ECS Trans.*, **111**, 349 (2023).
31. S. Dierickx, T. Mundloch, A. Weber, and E. Ivers-Tiffée, *ECS Trans.*, **78**, 1273 (2017).
32. T. Shimonosono, Y. Hirata, Y. Ehira, S. Sameshima, T. Horita, and H. Yokokawa, *Solid State Ionics*, **174**, 27 (2004) .
33. V. Sonn, A. Leonide, and E. Ivers-Tiffée, *J. Electrochem. Soc.*, **155**, B675 (2008).
34. A. Müller, A. Weber, H. J. Beie, A. Krügel, D. Gerthsen, and E. Ivers-Tiffée, *Proc. of the 3rd European Solid Fuel Cell Forum, Nantes, France, 1998, p. 353*.